



Cite this: DOI: 10.1039/d6tc00645k

# Chemical and physical pressure meet: deciphering the polymorphism and morphology of $\alpha$ - and $\delta$ -KY<sub>3</sub>F<sub>10</sub> induced by Eu<sup>3+</sup> doping

Samantha Custódio Silva Lemos,<sup>\*a</sup> Pablo Serna-Gallén,<sup>ib</sup> Lourdes Gracia,<sup>id</sup> <sup>\*ac</sup>  
Eduardo O. Gomes,<sup>a</sup> Héctor Beltrán-Mir,<sup>ib</sup> Eloísa Cordoncillo<sup>id</sup> and  
Juan Andrés<sup>\*a</sup>

An atomic-level understanding of the local effects on the structure and electronic properties provoked by chemical and/or physical pressure is essential; however, their intricate relationship is poorly understood, which poses a challenge for the design of new inorganic materials with tailored properties. In this work, we report the synthesis and comprehensive characterization of pure  $\alpha$ - and  $\delta$ -KY<sub>3</sub>F<sub>10</sub> polymorphs with varying Eu<sup>3+</sup>-doping levels (10–40%) revealing how the chemical (substitution of Y<sup>3+</sup> by Eu<sup>3+</sup>)–physical pressure effects can be separated to provide fundamental insight into the stability, electronic properties, and morphology of both polymorphs. Our results consist of XRD, ICP-MS, FT-IR, and HRSEM measurements in combination with DFT calculations. Experimental and theoretical findings disclose a coupling mechanism in  $\alpha$ - and  $\delta$ -KY<sub>3</sub>F<sub>10</sub> polymorphs, despite their otherwise near-identity, in which the negative pressure effect of the  $\delta$ -KY<sub>3</sub>F<sub>10</sub> polymorph is accompanied by subtle structural distortions and changes in the electronic configuration associated with a shift in the local coordination of Eu<sup>3+</sup> at the [EuF<sub>8</sub>] cluster from C<sub>2v</sub> to C<sub>4v</sub> symmetry. We assess the local atomic arrangements and stability of the (100), (110) and (111) surfaces of both polymorphs. The morphologies observed in the HRSEM images and the expected pathways and corresponding barrier heights connecting them are reproduced with remarkable accuracy. This work provides mechanistic insights into the transition between  $\alpha$ - and  $\delta$ -KY<sub>3</sub>F<sub>10</sub> polymorphs at low concentrations of Eu<sup>3+</sup>-doping and offers a theoretical basis to disentangle the chemical and physical pressure, providing a novel perspective for the rational design of high-performance KY<sub>3</sub>F<sub>10</sub>-based structures.

Received 1st March 2026,  
Accepted 27th April 2026

DOI: 10.1039/d6tc00645k

rsc.li/materials-c

## 1. Introduction

Crystal structures of inorganic materials can present different polymorphs with the same chemical composition, and often exhibit different physical properties, depending on how they were synthesized or the conditions under which they operate, such as pressure, temperature, doping, and so on.<sup>1</sup> Polymorphism is a common phenomenon of these crystalline materials, and in recent years, the discovery not only of the stability and functionality of new phases but also their capacity to undergo phase transitions is therefore particularly important in the development of materials in diverse scientific and industrial fields.<sup>2</sup>

Pressure, like temperature, is a fundamental thermodynamic variable that plays an important role in inducing structural transitions by tuning the lattice of inorganic materials to obtain metastable polymorphs with unusual properties that are otherwise not evident under ambient conditions.<sup>3–9</sup> Such metastable phases have emerged as a promising class of materials, thanks to their unique electronic structures, distinctive chemical bonding, and specific morphologies, which ultimately enable the realization of novel functions and applications.<sup>10–12</sup> However, the development of metastable phases still faces great challenges due to their native thermodynamic instability, calling for innovative synthetic methods and design strategies.<sup>13</sup> From the experimental side, high-pressure experiments, while enormously powerful, are limited not only by the high cost, but also by the low yields of metastable phases with larger volumes (lower density), making it hard to realize large-batch production for applications.<sup>14,15</sup>

On the other hand, chemical pressure associated with substitution or doping processes is the most common approach to

<sup>a</sup> Department of Physical and Analytical Chemistry, Universitat Jaume I, Av. Vicent Sos Baynat s/n, 12071, Castelló de la Plana, Spain

<sup>b</sup> Department of Inorganic and Organic Chemistry, Universitat Jaume I, Av. Vicent Sos Baynat s/n, 12071, Castelló de la Plana, Spain

<sup>c</sup> Department of Physical Chemistry, University of Valencia (UV), 46100 Burjassot, Spain



modify the intrinsic structure and properties of inorganic materials while changing their composition *via* lattice strain due to the different atomic radii and electronic and/or magnetic behaviors of the cations involved in the substitution process, which is realized by a chemical method instead of a physical one, and thus has an important influence on material properties.<sup>16–20</sup> In particular, the incorporation of a larger ion leads to an expansion of the crystal lattice, an effect equivalent to an effective negative external pressure, in the sense that it produces a structural dilation analogous to that generated by a decrease in the applied hydrostatic pressure. Application of both types of pressure allows not only tuning the physicochemical properties of materials by changing chemical interactions and modifying the electronic structure, but also induces phase transitions leading to new polymorphs with enhanced or novel functional properties.<sup>21,22</sup> In this connection, detailed knowledge of local lattice distortions and the respective effects of chemical and physical pressure when they are applied to inorganic materials is of major importance.<sup>23,24</sup> However, no adequate experimental and theoretical tools have been described in the literature so far.

Chemical and physical pressure often compete or coexist along the substitution process. While it is possible to resolve both, their innate complexity makes it nontrivial to unambiguously assign one to the other. Specifically, a comprehensive picture capturing the phenomena at play and the underlying rules that govern chemistry and physics is still under development. By using density functional theory (DFT) calculations, we have previously correlated chemical pressure with physical pressure, and investigated how the structural and electronic properties are modified by the formation of solid solutions, involving different semiconductors based on complex metal oxides, such as  $\text{NiW}_{1-x}\text{Mo}_x\text{O}_4$  ( $x = 25, 50, \text{ and } 75\%$ )<sup>25</sup> and  $\alpha\text{-Ag}_{2-2x}\text{Cu}_x\text{WO}_4$  ( $0 \leq x \leq 0.16$ ).<sup>26</sup> In this scenario, we were capable of disentangling the interactions associated with the doping process, from those arising from the pressure during the formation of the  $\text{SnMo}_{1-x}\text{W}_x\text{O}_4$  ( $x = 0\text{--}1$ ) solid solution,<sup>20</sup> and additionally, we performed controlled synthesis of the different polymorphs of  $\text{Ag}_2\text{WO}_4$ .<sup>27</sup> On the other hand, we have developed a method to obtain the available morphologies of a given material and applied it to investigate the crystal growth mechanisms, catalytic activity, and photoluminescence emissions.<sup>28–30</sup> Despite remarkable findings based on experimental structural characterization techniques, there are still open questions concerning polymorphism and morphology, including but not limited to cation distribution, bonding state, structural transformation, and morphological changes in many cases, material-specific.

A particularly important class of materials is the yttrium fluoride family that possesses a plethora of stoichiometries and a wide variety of ionic metal-fluorine bonding, as can be found in crystallography databases.<sup>31–34</sup> This diversity facilitates the possibility of tuning their physical and chemical properties, as their study has driven development in different applications over the last few years.<sup>35,36</sup> Among them, recent literature has highlighted renewed interest in potassium yttrium fluoride

( $\text{KY}_3\text{F}_{10}$ ) with numerous studies exploring its polymorphism to tailor its optical and electronic properties, such as magnetic resonance imaging,<sup>37</sup> biosensing,<sup>38</sup> theranostics<sup>39</sup> and high thermal sensitivity and upconversion luminescence, making it a prime candidate for advanced photonic applications.<sup>40,41</sup> In addition, electrical and dielectric investigations of the conduction processes in  $\text{KY}_3\text{F}_{10}$  crystals have been reported.<sup>42</sup>  $\text{KY}_3\text{F}_{10}$  presents two polymorphs with cubic structures, although with different space groups: the  $\alpha$ -phase belongs to  $Fm\bar{3}m$  (225), with 8 formula units per unit cell,  $Z = 8$ ,<sup>43</sup> while the  $\delta$ -polymorph belongs to  $Fd\bar{3}m$  (227) and has  $Z = 16$ . Both structures are composed of clusters of octahedrally arranged yttrium-centered square antiprisms [ $\text{YF}_8$ ], which share corners and edges to generate fluorine cubes and cuboctahedra.<sup>44</sup>

Beyond the scope of potential applications,  $\text{KY}_3\text{F}_{10}$  also serves as an excellent model of host systems. Previously, some of us were engaged in a research project to synthesize pure and  $\text{Eu}^{3+}$ -doped  $\text{KY}_3\text{F}_{10}$  crystal phases by different methods and to study the intriguing physics of their optical properties.<sup>45–47</sup> Polymorphism of  $\text{KY}_3\text{F}_{10}$  is complex, and controlling the crystallization of  $\alpha$ - and  $\delta$ -polymorphs is a challenge. The conditions that modulate their luminescence emissions by  $\text{Eu}^{3+}$  doping have also been identified, underscoring its advantage in accessing new structure–property regimes for rare-earth yttrium fluoride phosphors.<sup>48–50</sup> In addition, a transition between the  $\alpha/\delta$  polymorphs has been reported for  $\text{Eu}^{3+}$ -doped  $\text{KY}_3\text{F}_{10}$  compounds using different pH values of the reaction medium.<sup>51</sup> These differ only through the packing arrangement of local-range symmetry,  $C_{4v}$  and  $C_{2v}$ , due to the polar distortions of eight-coordinate  $\text{Eu}^{3+}$ -centered square antiprisms [ $\text{YEu}_8$ ], from becoming averaged out within  $\alpha$  and  $\delta$  crystals, respectively. The  $\delta$  polymorph was kinetically trapped as a result of the synthetic conditions; however, there are still many open questions about the underlying structural mechanisms, at the atomic scale, of the stabilization process. In addition, determining polymorph stability and phase transitions remains a major challenge in crystal structure prediction. The  $\alpha/\delta$ - $\text{KY}_3\text{F}_{10}$  polymorphs offer a unique opportunity to investigate the structural and electronic changes induced by the substitution of  $\text{Y}^{3+}$  by  $\text{Eu}^{3+}$  and physical pressure. Multiple routes to achieve phase control have been explored, such as cation exchange and pressure. While these routes have opened doors to phase manipulation, the former has limitations on which structures can be formed, and the latter does not directly target the product structure. Specifically, a comprehensive picture that captures the phenomena at play and the underlying rules that govern the  $\alpha/\delta$ - $\text{KY}_3\text{F}_{10}$  polymorphs and the analysis of morphological changes with the substitution of  $\text{Y}^{3+}$  by  $\text{Eu}^{3+}$  is still scarce. This requires new experimental and theoretical approaches to gain insight into the effects of chemical and physical pressure, which have not been assessed and compared in full detail.

To take further steps towards clarifying the intriguing relationship between  $\text{Eu}^{3+}$  doping (chemical pressure) and the physical pressure of pure and  $\text{Eu}^{3+}$ -doped  $\alpha$ -,  $\delta$ - $\text{KY}_3\text{F}_{10}$  polymorphs, this work aims to provide a sound response to this



question by focusing on the structure and stability of these polymorphs, quantifying their thermodynamic accessibility and the contribution of individual lattice sites. Studying them is a highly fruitful endeavor, while at the same time challenging. Bridging this knowledge gap necessitates the synergy of experimental measurements with robust DFT calculations for rationalizing experimental results and understanding material properties. Herein, X-ray diffraction (XRD), infrared (IR) spectroscopy, and inductively coupled plasma mass spectrometry (ICP-MS) were employed for structural and elemental analysis. Then, we further investigated their morphology by high-resolution scanning electron microscopy (HRSEM). A model based on the combination of calculated surface energies and Wulff construction is proposed to explain and predict the available morphologies of both polymorphs. An attempt was then made to establish a relationship between chemical and physical pressure based on the structural and morphological characterization results.

Therefore, the main aims of the present article are threefold: first, we will find how and where chemical and physical pressure meet in the  $\alpha$ - and  $\delta$ - $\text{KY}_3\text{F}_{10}$  polymorphs. Second, to unveil the influence of the spin configuration of the incorporated  $\text{Eu}^{3+}$  and disclose a correlation along the substitution process of  $\text{Y}^{3+}$  by  $\text{Eu}^{3+}$  between the pressure-induced phase transition and the negative linear compressibility of the  $\delta$ - $\text{KY}_3\text{F}_{10}$  polymorph. Third, the surface stability of various crystallographic surfaces of pure and doped  $\alpha$ - and  $\delta$ - $\text{KY}_3\text{F}_{10}$  polymorphs is assessed. Based on these findings, a map of available morphologies is constructed, which allows a close match between experimental HRSEM images and the computational thermodynamic model derived from the results of DFT calculations and Wulff construction.

## II. Results and discussion

$\alpha$ - and  $\delta$ -polymorphs can be described in terms of the minimal building block, *i.e.*, the  $[\text{YF}_8]$  cluster, in which the  $\text{Y}^{3+}$  central cation displays a  $C_{4v}$  and  $C_{2v}$  local symmetry, respectively. The cluster we chose for our study serves as an appropriate model to explore the degree of structural changes in both polymorphs,

which ultimately affects the stability with incorporated  $\text{Eu}^{3+}$  cations. A 3D representation of both  $\alpha$  and  $\delta$ - $\text{KY}_3\text{F}_{10}$  structures is presented in Fig. 1, in which the non-centrosymmetric  $\text{Eu}^{3+}$  site environment at the  $[\text{YF}_8]$  cluster is highlighted.

Before the detailed analysis of differences between the experimental data and model predictions, it is crucial to note here the assumptions made in our theoretical approach. First, taking into account hybrid functionals such as PBE0 to mitigate the self-interaction error present in GGA functionals and providing improved band-gap estimates.<sup>52,53</sup> Second, to enhance the accuracy of understanding and predicting in the high-spin structures within the PBE0 functional, yet its theoretical description poses a challenge for common excited-state methods. Despite facing challenges due to existing technical and theoretical constraints and given the typical uncertainties in experimentally measured atomic distances ( $\pm 0.01$  Å), a good agreement among measurements, previous reports, and calculated geometry (lattice parameters, bond distances, and angles) by using this functional is found (see Table 1). It is important to note the significant volume expansion of *ca.* 7.8% in the  $\delta$ - $\text{KY}_3\text{F}_{10}$  polymorph with respect to  $\alpha$ , associated with enlarged crystallographic repeat units (higher *Z*, from 8 to 16). In the calculated  $\alpha$ -phase, the  $[\text{YF}_8]$  square antiprism cluster is distorted, and hence, has four Y–F bond distances of 2.21 Å and four Y–F bond distances of 2.36 Å. The  $\delta$ -phase presents a more distorted local environment for the  $\text{Y}^{3+}$  cations; the  $[\text{YF}_8]$  square antiprism cluster has four Y–F bond distances of 2.24 Å, two with 2.31 Å and two with 2.36 Å, consistent with previous experimental results.<sup>54</sup> An analysis of the DFT-optimized structures points out a  $[\text{YF}_8]$  square antiprism flattening from the  $\alpha$  to the  $\delta$ -polymorph, leading to reduced symmetry, from  $C_{4v}$  to  $C_{2v}$ , respectively. Consequently, the material may exhibit local structural reorganization rather than a complete phase transition (with an energy difference between the two polymorphs of 0.306 eV), involving a shift from a distorted cubic structure  $Fm\bar{3}m$  to a more asymmetric  $Fd\bar{3}m$ .

The rare-earth cations,  $\text{Y}^{3+}$  and  $\text{Eu}^{3+}$ , share many comparable chemical and physical properties due to their similar oxidation states, electronegativity, and ionic radius (1.019 Å for  $\text{Y}^{3+}$  and 1.066 Å for  $\text{Eu}^{3+}$  with a coordination number = 8).<sup>55</sup> In addition, the electron configuration in the outer valence

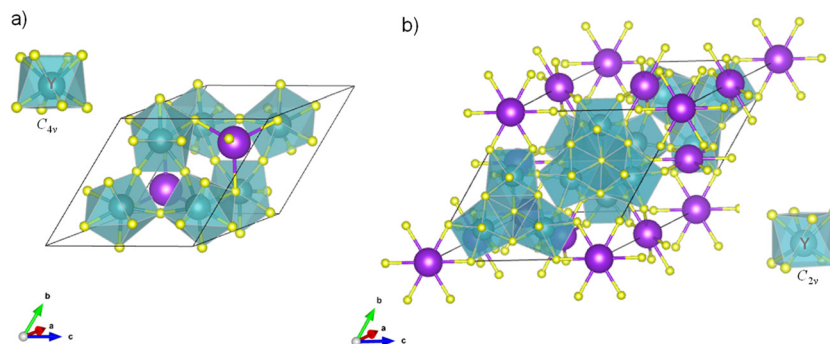


Fig. 1 3D illustration of  $\alpha$ - $\text{KY}_3\text{F}_{10}$  (a) and  $\delta$ - $\text{KY}_3\text{F}_{10}$  (b) structures, highlighting the local coordination of the  $\text{Y}^{3+}$  cation with  $C_{4v}$  and  $C_{2v}$  symmetry, respectively. The purple, blue, and yellow spheres represent the K, F, and Y atoms.



**Table 1** Experimental and calculated values of the geometry (cell parameters, bond lengths, and bond angles), band gap and total energy of  $\alpha$ - and  $\delta$ -KY<sub>3</sub>F<sub>10</sub> polymorphs

	Experimental <sup>59</sup>		Calculated
$\alpha$ -KY <sub>3</sub> F <sub>10</sub>			
Cell parameter (Å)	<i>a</i>	11.52	11.66
Cell volume (Å <sup>3</sup> )	<i>V</i>	1530.06	1587.41
Bond length (Å)	Y-F <sub>1</sub> (4)	2.19	2.21
	Y-F <sub>2</sub> (4)	2.34	2.36
Band gap (eV)			11.02
Total energy/f.u. (eV)			-31044.275
$\delta$ -KY <sub>3</sub> F <sub>10</sub>			
Cell parameter (Å)	<i>a</i>	15.48	15.56
Cell volume (Å <sup>3</sup> )	<i>V</i>	3711.70	3764.51
Bond length (Å)	Y-F <sub>1</sub> (4)	2.21	2.24
	Y-F <sub>2</sub> (2)	2.29	2.31
	Y-F <sub>3</sub> (2)	2.39	2.36
Band gap (eV)			11.22
Total energy/f.u. (eV)			-31043.969

shell is Y<sup>3+</sup>-[Kr] while Eu<sup>3+</sup> has additional 4f orbitals that fill up after the [Xe] shell, *i.e.*, Eu<sup>3+</sup>-[Xe] 4f<sup>6</sup>. Hence, their introduction does not create oxygen vacancies in the structure because charge balancing is maintained. The nominal percentages of Eu<sup>3+</sup> used were: 10, 15, 20, 30, 40, 50, and 100 mol% with respect to the total amount of Ln (Ln = Y and Eu). Samples were denoted as “S-*n*”, where *n* indicates the percentage of Eu<sup>3+</sup>. The XRD analysis of Eu<sup>3+</sup>-doped samples (up to 40 mol% Eu<sup>3+</sup>) provides insight into their structural characteristics. As shown in Fig. 2, in which the XRD cards of cubic  $\delta$ -KY<sub>3</sub>F<sub>10</sub>·*x*H<sub>2</sub>O (ICSD card 04-016-7073), cubic  $\alpha$ -KY<sub>3</sub>F<sub>10</sub> (ICSD card 00-040-9643), and orthorhombic YF<sub>3</sub> (ICDD card 00-032-1431) have been included to serve as references; the sharp and intense peaks suggest high crystallinity with well-defined lattice planes. The XRD patterns of sample S-10 (10 mol% Eu<sup>3+</sup>) unequivocally demonstrate the phase purity of the synthesized sample, with solely exhibiting the characteristic of  $\delta$ -phase, with no traces or impurities of other crystal structures. Low-intensity peaks corresponding to the  $\alpha$ -phase appear in the XRD pattern of sample S-15 (15 mol% Eu<sup>3+</sup>), being more prominent as the Eu<sup>3+</sup> content increases. Indeed, the presence of both  $\alpha$ - and  $\delta$ -phases is very clear in sample S-30 (30 mol% Eu<sup>3+</sup>). The same peaks are present without additional peaks corresponding to europium oxides. The absence of secondary phases suggests that Y<sup>3+</sup> cations are successfully substituted by Eu<sup>3+</sup> within the lattice, rather than forming separate europium oxide compounds; however, higher percentages of the Eu<sup>3+</sup> induce the presence of secondary phases, which can be ascribed to YF<sub>3</sub> (see sample S-40), being more evident at higher percentages of Eu<sup>3+</sup> (samples S-50 and S-100), as it is presented in the SI. The incorporation of Eu<sup>3+</sup> into the KY<sub>3</sub>F<sub>10</sub> matrix induces lattice strain, evident from the slight broadening of diffraction peaks.

Fig. S1 in the SI shows the XRD patterns of samples S-50 and S-100, mainly composed of YF<sub>3</sub>, hexagonal EuF<sub>3</sub>, and orthorhombic EuF<sub>3</sub> phases.

The IR spectra of the prepared samples are presented in Fig. 3. In the low-energy region, 200–600 cm<sup>-1</sup> (Fig. 3b), prominent bands are observed for S30 and S40 samples at 231, 276,

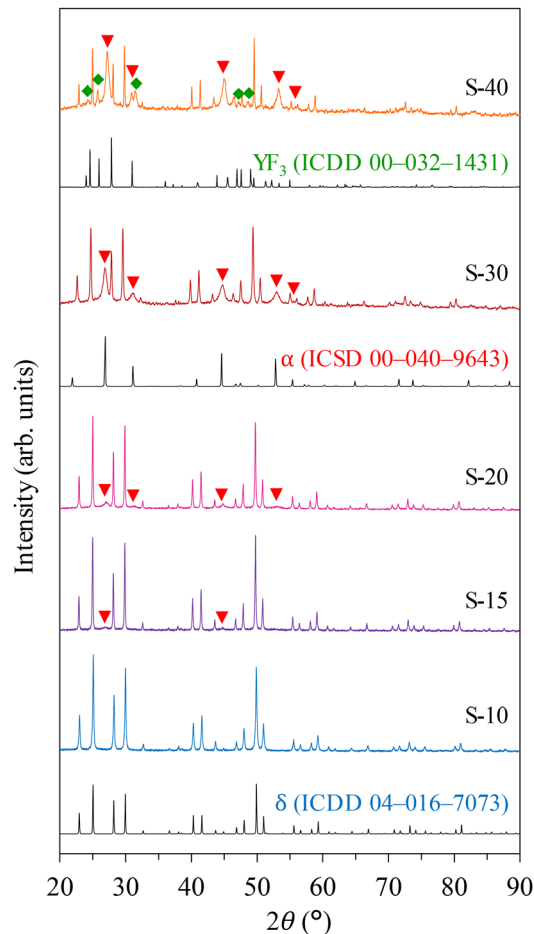


**Fig. 2** XRD patterns of samples doped with Eu<sup>3+</sup> in the range 10–40 mol%. The peaks indicated with red triangles are associated with the  $\alpha$ -phase, while those highlighted with green diamonds refer to the presence of orthorhombic YF<sub>3</sub>.

and 364 and 500 cm<sup>-1</sup>, assigned to  $\alpha$ -KY<sub>3</sub>F<sub>10</sub> structure, while the bands at 215, 241, and 295 and 395 cm<sup>-1</sup> for S10, S15, and S20 samples correspond to the  $\delta$ -KY<sub>3</sub>F<sub>10</sub> structure. The calculated IR spectra for the pure (black) and doped (colored)  $\alpha$  and  $\delta$  phases can be seen in Fig. 3c. The IR frequencies of the prepared samples (S10 and S20), as well as the calculated IR frequencies of  $\alpha$  and  $\delta$ -KY<sub>3</sub>F<sub>10</sub> polymorphs at 16.7% and 8.3% of Eu<sup>3+</sup> doping, are presented in Table S2 of the SI. The  $\alpha$ -KY<sub>3</sub>F<sub>10</sub> structure exhibits 8 IR-active (8T<sub>1u</sub>) modes according to group theory analysis. The calculated IR spectra of  $\alpha$ -KY<sub>3</sub>F<sub>10</sub> depict, as principal contributions, bands at 243, 315, and 360 cm<sup>-1</sup> assigned to Y-F-K, F-Y-K, and F-Y-F bending modes, respectively, and a band at 508 cm<sup>-1</sup> associated with the F-Y stretching mode. The  $\delta$ -KY<sub>3</sub>F<sub>10</sub> structure exhibits 14 IR-active (14T<sub>1u</sub>) modes according to group theory analysis. In the calculated spectra of  $\delta$ -KY<sub>3</sub>F<sub>10</sub> bands attributed to the bending of F-Y-F, F-Y-K, F-Y-F, and F-Y-K were observed at 228, 255, 288, and 324 cm<sup>-1</sup>, respectively, and a F-Y stretching mode was observed at 414 cm<sup>-1</sup>. When Y<sup>3+</sup> is substituted by Eu<sup>3+</sup>, new vibrational modes appear due to a symmetry-breaking process. The overlap of peaks (leads to band broadening and shifts



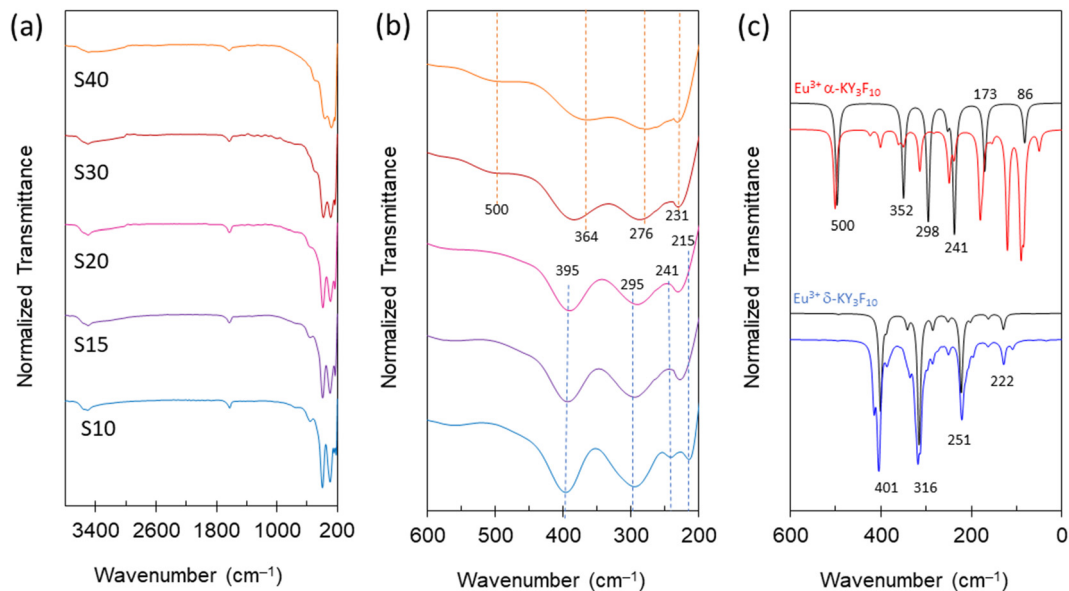


Fig. 3 Experimental IR spectra of samples (a), amplified region of the spectra in the range 200–600  $\text{cm}^{-1}$  (b), and the calculated IR spectra for the  $\alpha$  and  $\delta$  crystal phases, pure (black) and doped (colored) (c). The dashed lines in (b) serve as guidelines to observe the change in the position and presence of some peaks of interest.

towards lower frequencies due to subtle structural changes resulting from the  $\text{Eu}^{3+}$  doping.

Next, we carry out an extensive structural optimization of  $\text{Eu}^{3+}$ -doped  $\alpha$  and  $\delta$  crystalline  $\text{KY}_3\text{F}_{10}$  polymorphs at different spin multiplicities of 5 and 7, which are denoted as  $M = 5$  and  $M = 7$ , respectively. The calculated values of the geometry, band gap, and total energy of  $\alpha$ - and  $\delta$ - $\text{KY}_3\text{F}_{10}$  polymorphs at 8.3% and 16.7% of  $\text{Eu}^{3+}$  doping are presented in Tables 2 and 3, respectively. The substitution process is associated with a comparable energetic cost in both structures, with a very small difference of approximately 0.004 eV, suggesting that  $\text{Eu}^{3+}$  incorporation does not strongly favor one phase over the other from a purely energetic standpoint. Therefore, the concept of chemical pressure can be interpreted as arising primarily from local structural distortions induced by the size and electronic differences between  $\text{Eu}^{3+}$  and  $\text{Y}^{3+}$ , rather than from a large energetic driving force for substitution. The variation in bond

distances around the substituted  $\text{Y}^{3+}$  by  $\text{Eu}^{3+}$  implies subtle distortions in the local environment at the  $[\text{EuF}_8]$  cluster in both  $\alpha$  and  $\delta$  polymorphs (Eu–F distances ranged from 2.26 to 2.40 Å and 2.28 to 2.39 Å, respectively). Considering this induction of a local strain and a cluster expansion, a possible phase transition to a phase with expanded volume would be expected (an effect equivalent to an effective negative external pressure).

The energy–volume curves of the different polymorphs are presented in Fig. 4a, where arrows from the bottom to the top herein indicate phases connected across these transitions. For  $\text{KY}_3\text{F}_{10}$ , negative pressure enhances the distortion of the  $[\text{YF}_8]$  square antiprism cluster and induces a less symmetrical environment for  $\text{Y}^{3+}$  cations in passing from the  $\alpha$  to the  $\delta$  phase. Therefore, from the structural point of view, substituting  $\text{Y}^{3+}$  by  $\text{Eu}^{3+}$  cations (chemical pressure) provides an efficient way to expand crystalline structures. As compressions are commonly related to positive pressures and the opposing effects of pressure and temperature, it is interesting to use the concept of chemical pressure to offer a unified view of the entire phenomenon.<sup>7</sup> An attempt is made to link the experimental observation of a symmetry reduction, *i.e.*, the structural motif of the square antiprism with  $C_{4v}$  symmetry, to a square antiprism with  $C_{2v}$  symmetry. In comparison, the  $C_{2v}$  local coordination is preferred at 8.3%  $\text{Eu}^{3+}$ , according to our calculations and in agreement with the experimentally observed overall substitution. We estimate the enthalpy variation as a function of physical pressure, as shown in Fig. 4b. This thermodynamic analysis provides a deep understanding of crystalline metastability and can be a foundation on which future kinetic theories, involving transformation barriers and metastable lifetimes, can be constructed. An analysis of the results indicates an  $\alpha$  ( $Fm\bar{3}m$ ) to  $\delta$  ( $Fd\bar{3}m$ ) phase transition at a

Table 2 Calculated values of the cell parameters and bond lengths, band gap, and total energy of  $\alpha$ - and  $\delta$ - $\text{KY}_3\text{F}_{10}$  polymorphs at 8.3% of  $\text{Eu}^{3+}$  doping and spin multiplicities  $M = 7$  and  $M = 5$  and 7, respectively

		8.3% Eu doped	
$\alpha$ - $\text{KY}_3\text{F}_{10}$		$M = 7$	
Cell volume ( $\text{\AA}^3$ )	$V$	1595.78	
Bond length ( $\text{\AA}$ )	Eu–F <sub>1</sub>	2.26 (2) 2.27 (2)	
	Eu–F <sub>2</sub>	2.37(1) 2.39(1) 2.40(2)	
		4.24/8.94	
Band gap (eV)		4.24/8.94	
Total energy/f.u. (eV)		–35617.900	
$\delta$ - $\text{KY}_3\text{F}_{10}$		$M = 5$	
Cell volume ( $\text{\AA}^3$ )	$V$	3783.56	
Bond length ( $\text{\AA}$ )	Eu–F <sub>1</sub> (4)	2.28	
	Eu–F <sub>2</sub> (2)	2.36	
	Eu–F <sub>3</sub> (2)	2.38	
		2.39	
Band gap (eV)	$\alpha/\beta$	7.48/4.85	
Total energy/f.u. (eV)		–35616.868	
		$M = 7$	
		3782.98	
		2.28	
		2.35	
		2.39	
		4.94/9.03	
		–35617.595	



**Table 3** Calculated values of the geometry (cell parameters and bond lengths), band gap, and total energy of  $\alpha$ - and  $\delta$ -KY<sub>3</sub>F<sub>10</sub> polymorphs at 16.7% of Eu<sup>3+</sup> doping at spin multiplicity  $M = 7$

		16.7% Eu doped	
$\alpha$ -KY <sub>3</sub> F <sub>10</sub> supercell		$M = 7$	
Cell volume (Å <sup>3</sup> )	$V$	1604.14	
Bond length (Å)	Eu–F <sub>1</sub>	2.26 (2)	2.27 (2)
	Eu–F <sub>2</sub>	2.39 (3)	2.40 (1)
Band gap (eV)	$\alpha/\beta$	5.5/6.65	
Total energy/f.u. (eV)		–40191.389	
$\delta$ -KY <sub>3</sub> F <sub>10</sub>		$M = 7$	
Cell volume (Å <sup>3</sup> )	$V$	3802.73	
Bond length (Å)	Eu–F <sub>1</sub> (4)	2.29	
	Eu–F <sub>2</sub> (2)	2.35	
	Eu–F <sub>3</sub> (2)	2.39	
Band gap (eV)	$\alpha/\beta$	4.80/9.04	
Total energy/f.u. (eV)		–40191.198	

negative pressure value of  $-1.2$  GPa, indicating that for this transition, the volume of the involved structures is expanded. In addition, other possible phase transitions have been explored, starting from the  $\alpha$  phase: when a positive pressure is applied, a phase transition to a tetragonal structure ( $P4_2/mmc$ )<sup>56</sup> takes place at 15 GPa, and a phase transition  $\alpha$  to the rhombohedral structure ( $R3m$ ), material ID mp-34042, is observed at a high negative pressure, indicating that high temperature is needed for this transformation. The mechanism of this phase transition can be classified as a pressure-induced collapse caused by reorientation and a shift toward tighter space-filling. In addition, the phase transition from the  $\alpha$  to the  $\delta$  phase at  $-1.2$  GPa, is maintained at 8.3% and 16.7% of Eu<sup>3+</sup> doping (see Fig. S2 of the SI).

In accordance with Hund's rule of maximum multiplicity, Eu<sup>3+</sup> presents a high spin such that the potential energy required to maintain a high spin configuration surpasses the spin pairing energy.<sup>57,58</sup> In our case,  $\alpha$  and  $\delta$  Eu<sup>3+</sup>-doped KY<sub>3</sub>F<sub>10</sub> structures are dominated by ionic interactions (closed-shell F<sup>–</sup> and Eu<sup>3+</sup>), which are in the meV order. The corresponding global minimum of the  $\alpha$  and  $\delta$  polymorphs is located at the same high spin multiplicity. Moreover, in comparison to the 5d orbital, the 4f orbitals of Eu<sup>3+</sup> possess no significant overlap

with F<sup>–</sup> orbitals. As a consequence, the 4f electrons scarcely delocalize onto the F<sup>–</sup> orbitals, and these interactions are not capable of breaking the degeneracy of the Eu<sup>3+</sup> cation-4f orbitals in the [EuF<sub>8</sub>] cluster of the  $\alpha/\delta$ -KY<sub>3</sub>F<sub>10</sub> polymorphs.

An extensive exploration of the stable configurations at different spin multiplicities is performed for both polymorphs. For the  $\alpha$ -KY<sub>3</sub>F<sub>10</sub> polymorph at 8.3% and 16.7% Eu<sup>3+</sup>, only a minimum with a spin multiplicity of 7 (6 unpaired electrons at the 4f orbitals) is found (see Tables 2 and 3). The  $\delta$ -KY<sub>3</sub>F<sub>10</sub> polymorph, doped with 8.3%-Eu<sup>3+</sup>, presents two minima, a high-spin 7 (6 unpaired electrons at the 4f orbitals) and a moderate-spin 5 (4 unpaired electrons). The relative stability between the  $\alpha$  and  $\delta$ -KY<sub>3</sub>F<sub>10</sub> polymorphs at 8.3% and 16.7% Eu<sup>3+</sup> for the most stable structures with  $M = 7$  are 0.30 and 0.19 eV, respectively. This observation indicates the possibility for the simultaneous formation of both pure and doped polymorphs, as it appears in S-15, S-20, and S-30 (see Fig. 2), or the energy required for phase transition can be achieved at relatively lower temperatures. In addition, the  $\delta$ -KY<sub>3</sub>F<sub>10</sub> polymorph presents an energy between the  $M = 7$  and  $M = 5$  of 0.63 eV. Different configurations involving the two Eu<sup>3+</sup> substitutions at different relative positions (16.7%) were systematically examined, showing negligible total energy differences (see Table S3 and its discussion in the SI).

To gain insight into the electronic properties of pure and Eu<sup>3+</sup>-doped  $\alpha$  and  $\delta$ -KY<sub>3</sub>F<sub>10</sub> polymorphs, we analyze the corresponding changes in the density of states (DOS) projected on atoms and orbitals. Fig. S3(a) in the SI shows that both polymorphs present a wide band gap material, with the valence band (VB) being predominantly composed of F 2p orbitals, while the conduction band (CB) is from Y 4d orbitals, with a band gap for  $\delta$ - and  $\alpha$ -polymorphs of 11.2 and 11.0 eV, respectively. The projected DOS on the orbitals of K<sup>+</sup>, F<sup>–</sup>, Y<sup>3+</sup> and Eu<sup>3+</sup> ions for the  $\alpha$ -phase at 8.3% Eu ( $M = 7$ ),  $\alpha$ -phase at 16.7% Eu ( $M = 7$ ),  $\delta$ -phase at 8% Eu ( $M = 5$ ),  $\delta$ -phase at 8.3% Eu ( $M = 7$ ) and  $\delta$ -phase at 16.7% Eu ( $M = 7$ ) are depicted in Fig. S3(b–f), respectively. The resulting modifications in the DOS and band gap offer a qualitative understanding of the conductivity variations observed upon Eu<sup>3+</sup> doping, as these directly influence

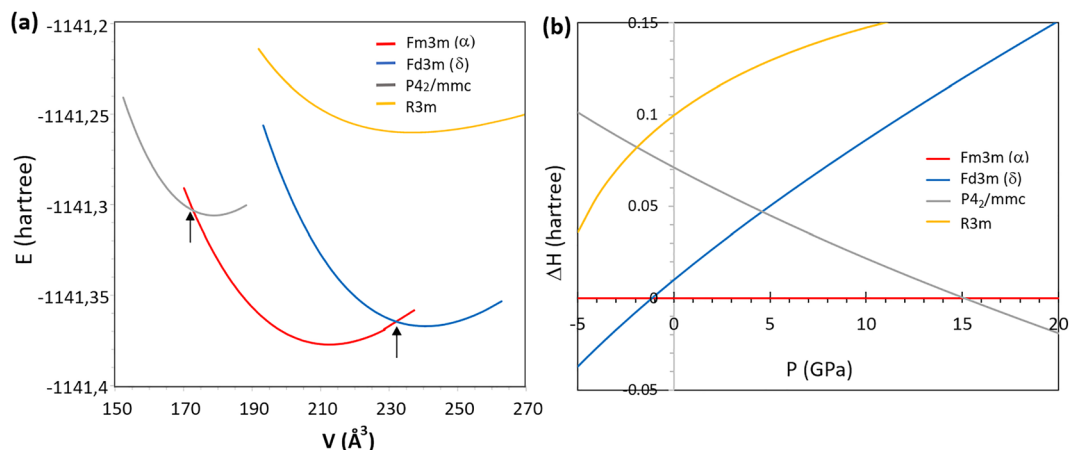


**Fig. 4** Energy–volume curves of the different studied polymorphs (a). Enthalpy variation as a function of pressure (b).



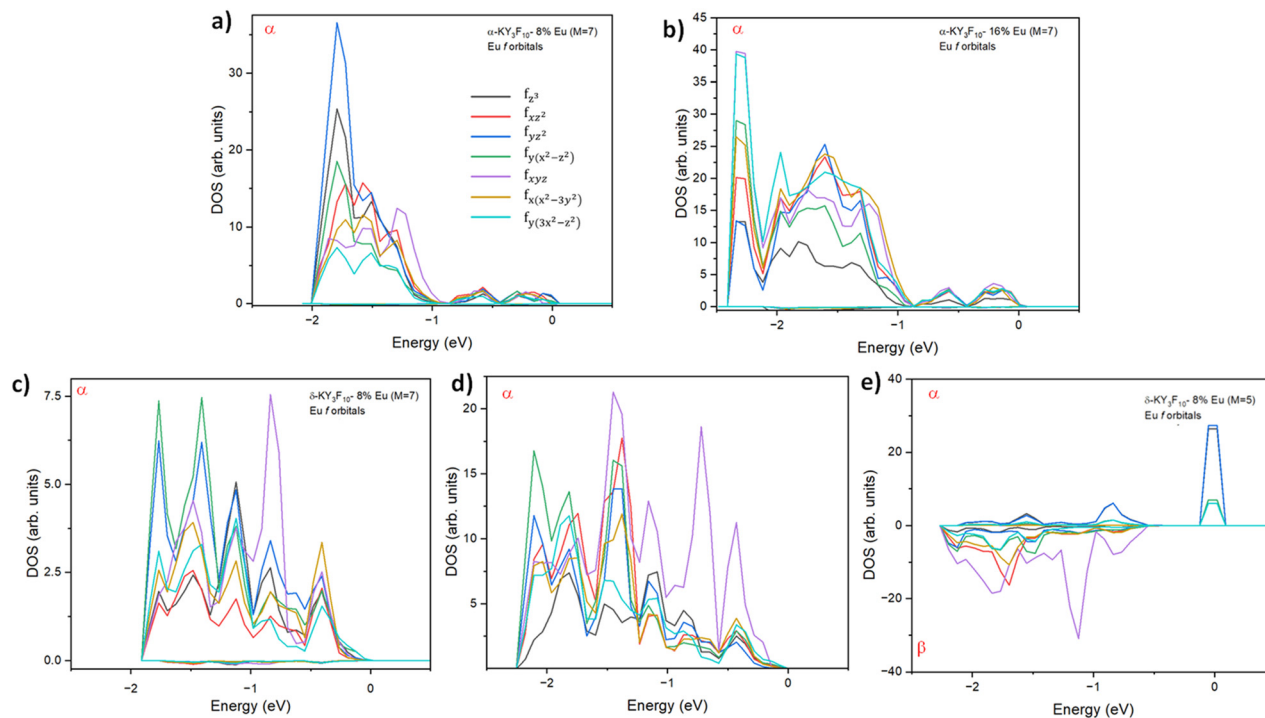


Fig. 5 Projected DOS on the f orbitals of  $\text{Eu}^{3+}$  for the  $\alpha$ -phase: (a) 8.3% Eu ( $M = 7$ ) and (b) 16.7% Eu ( $M = 7$ ); for the  $\delta$ -phase: (c) 8.3% Eu ( $M = 5$ ), (d) 8.3% Eu ( $M = 7$ ), and (e) 16.7% Eu ( $M = 7$ ). A vertical dashed line indicates the Fermi level. Spin-up and spin-down electrons are denoted  $\alpha$  and  $\beta$ .

carrier availability and transport properties. For the  $\text{Eu}^{3+}$ -doped systems (where the spin-up and spin-down electrons are denoted with  $\alpha$  and  $\beta$ , respectively), it is observed that the presence of localized intermediate states, at the band gap, formed by empty Eu 4f orbitals, substantially modifies the DOS, enhancing the optical absorption in the visible region and electronic conductivity of both polymorphs. In general, the values of the band gap decrease to 4.2 eV at 8.3%  $\text{Eu}^{3+}$  ( $M = 7$ ) and up to 5.5 eV at 16.7%  $\text{Eu}^{3+}$  (for  $M = 7$ ) for the  $\alpha$ -phase. For the  $\delta$ -phase, the gap is reduced to 4.8 eV at 8.3%  $\text{Eu}^{3+}$  for  $M = 5$ , to 4.9 eV for  $M = 7$ , and to 4.8 eV at 16.7%  $\text{Eu}^{3+}$ .

Fig. 5 illustrates the projected DOS on the f orbitals of  $\text{Eu}^{3+}$  and their contribution in the VB region. An analysis of Fig. 5a and b shows that the VBs at 8.3%  $\text{Eu}^{3+}$  are mainly contributed by the half-filled  $f_{yz^2}$  orbital (40%) while at 16.7%  $\text{Eu}^{3+}$  are composed by the combination (60%) of half-filled  $f_{xyz}$  and  $f_{y(3x^2-z^2)}$  orbitals. Its percentage of contribution was determined by calculating the area below the curve corresponding to the 4f orbitals in the VB of the DOS. An analysis of Fig. 5c and d of the  $\delta$ -polymorph renders that the VB at 8.3% with high spin ( $M = 7$ ) is mainly composed of half-filled  $f_{y(x^2-z^2)}$  (35%) and to a minor extent by half-filled  $f_{xyz}$  (30%), while at 16.7%  $\text{Eu}^{3+}$ , by half-filled  $f_{xyz}$  (50%). At 8.3%  $\text{Eu}^{3+}$  with moderate spin ( $M = 5$ ), the VB is mainly composed of the filled  $f_{xyz}$  orbital (45%), while the half-filled  $f_{xz^2}$  (15%) and each  $f_{yz^2}$ ,  $f_{y(x^2-z^2)}$ ,  $f_{y(3x^2-y^2)}$  orbitals contributed to 10%, as it is depicted in Fig. 5e. These results are schematically presented in Fig. S4 in the SI, in which the electron configurations for the 4f orbitals are depicted for the  $C_{4v}$  and  $C_{2v}$  symmetry of the  $[\text{EuF}_8]$  site. The  $C_{4v}$  symmetry at

8.3%  $\text{Eu}^{3+}$  and 16.7%  $\text{Eu}^{3+}$  presents an electronic configuration with major contributions from the half-filled  $f_{yz^2}$  and  $f_{xyz}$ ,  $f_{y(3x^2-z^2)}$  orbitals, respectively. For the 4f orbitals at the  $C_{2v}$  symmetry of the  $\delta$  phase, the f orbital contribution to the VB depends not only on the  $\text{Eu}^{3+}$  doping concentration but also on the multiplicity. The  $C_{2v}$  symmetry at 8.3% and 16.7%  $\text{Eu}^{3+}$  with  $M = 7$  has an electronic configuration with major contributions from the half-filled  $f_{y(x^2-z^2)}$  and  $f_{xyz}$  orbitals, respectively, while at 8.3%  $\text{Eu}^{3+}$  with  $M = 5$  the most contributed orbital is the filled  $f_{xyz}$ . Moreover, the  $\text{Eu}^{3+}$  doping process alters the electronic structure and band alignment of the  $\alpha$  and  $\delta$  phases of  $\text{KY}_3\text{F}_{10}$ , thereby causing a transition in the configuration and occupancy of the f orbitals of  $\text{Eu}^{3+}$  at the  $C_{4v}$  and  $C_{2v}$  symmetry of the  $[\text{EuF}_8]$  cluster in the  $\alpha$  and  $\delta$ -polymorphs. Finally, it is interesting to note that the empty Eu 4f orbitals constitute localized intermediate states at the band gap, follow similar contributions and can be well correlated with the composition of occupied Eu 4f orbitals of VB.

The morphologies of the as-prepared samples, S-10, S-15, S-20, S-30, and S-40, obtained using HRSEM, are presented in Fig. 6. An analysis of the results presented herein indicates that the nanoparticles have homogeneous distribution, good dispersion, and only small differences in average size upon  $\text{Eu}^{3+}$  doping. However, diverse morphologies are found, which are driven by the variation of  $\text{Eu}^{3+}$  content, from spherical in S-10 to octahedral at S-15, with a dominant (111) surface. In S-20, a cubic morphology is observed, which is composed mainly of the (100) surface, while a truncated octahedra morphology is found at the S-30 sample, in which the (111) and



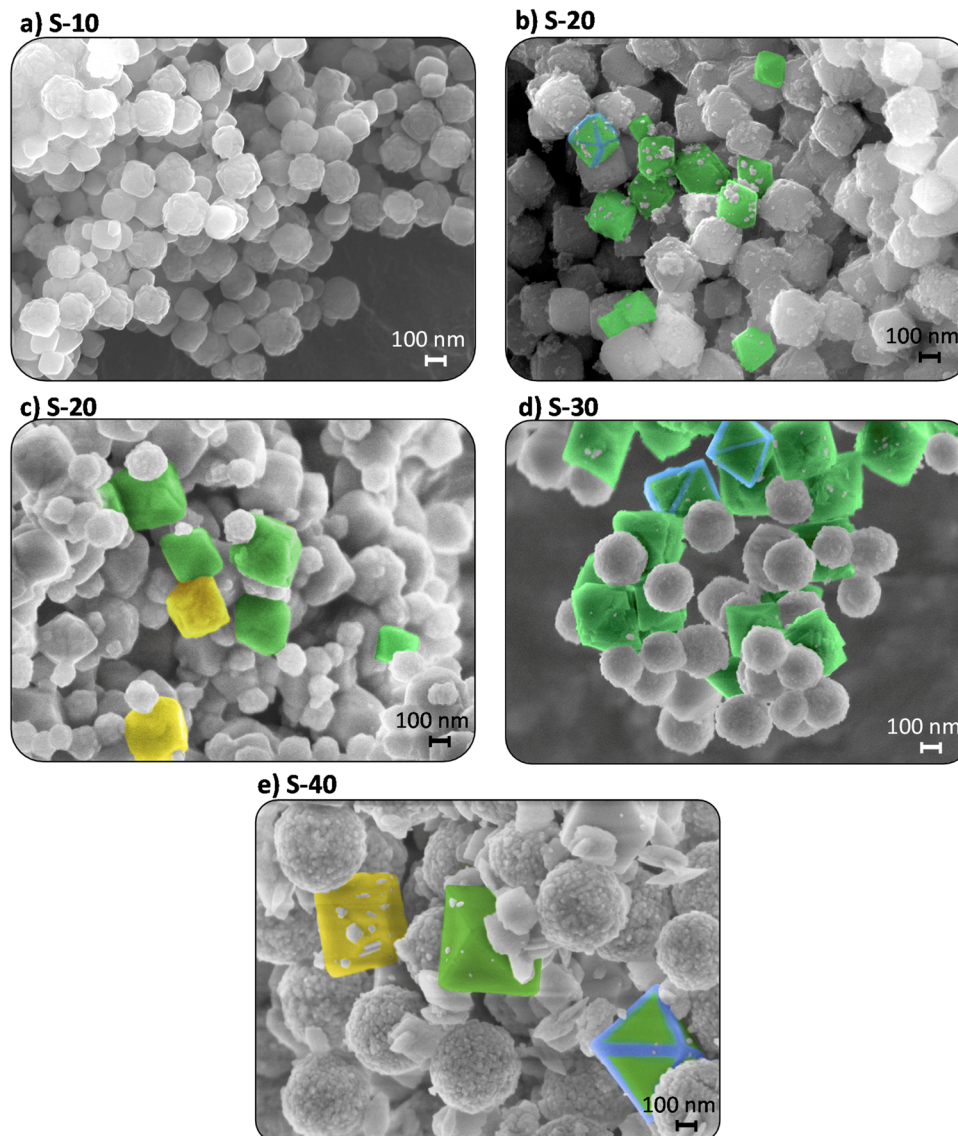


Fig. 6 HRSEM images of (a) S-10, (b) S-15, (c) S-20, (d) S-30, and (e) S-40 samples. Well-defined morphologies have been pointed out in each image, and the corresponding models of octahedron, truncated octahedron, and a cube are highlighted for comparison purposes.

(110) surfaces are predominant. Lastly, in S-40, a complete set of morphologies (octahedra, truncated octahedra, and cubic) can be observed.

To accurately evaluate the formation energies of different crystal surfaces, a typical slab model was used in the calculations. This model is constructed by selectively exposing the plane of interest and removing a portion of the atoms to form a vacuum. All slab models are constrained to the symmetrical top and bottom surfaces. The values of  $E_{\text{surf}}$  can be calculated by eqn (1):

$$E_{\text{surf}} = \frac{[E_{\text{slab}} - n \cdot E_{\text{bulk}}]}{2A} \quad (1)$$

where  $E_{\text{slab}}$  and  $E_{\text{bulk}}$  are the total energies of the surface slab model and the bulk (unit cell), respectively;  $n$  refers to the number of bulk units in the slab, and  $A$  is the surface area for

symmetric slabs. The slab surface models are stoichiometric and the convergence of the calculated surface energies with the number of layers in the slab model was examined. The broken bond density ( $D_B$ ) of the surface was calculated using eqn (2), in which  $n_{\text{BB}}$  is the number of broken bonds in the termination and  $A$  is the surface area

$$D_B = \frac{n_{\text{BB}}}{A} \quad (2)$$

The polyhedron energy,  $E_{\text{pol}}$ , is calculated using eqn (3):

$$E_{\text{pol}} = \sum C_i \times E_{\text{surf}} \quad (3)$$

where  $C_i$  is the percentage of contribution of the surface area to the total area of the polyhedron,  $C_i = A^i/A^{\text{pol}}$ .<sup>59</sup>

The (100), (110) and (111) surface models for  $\alpha$ - and  $\delta$ -KY<sub>3</sub>F<sub>10</sub> are presented in Fig. 7. An analysis of Y and K superficial



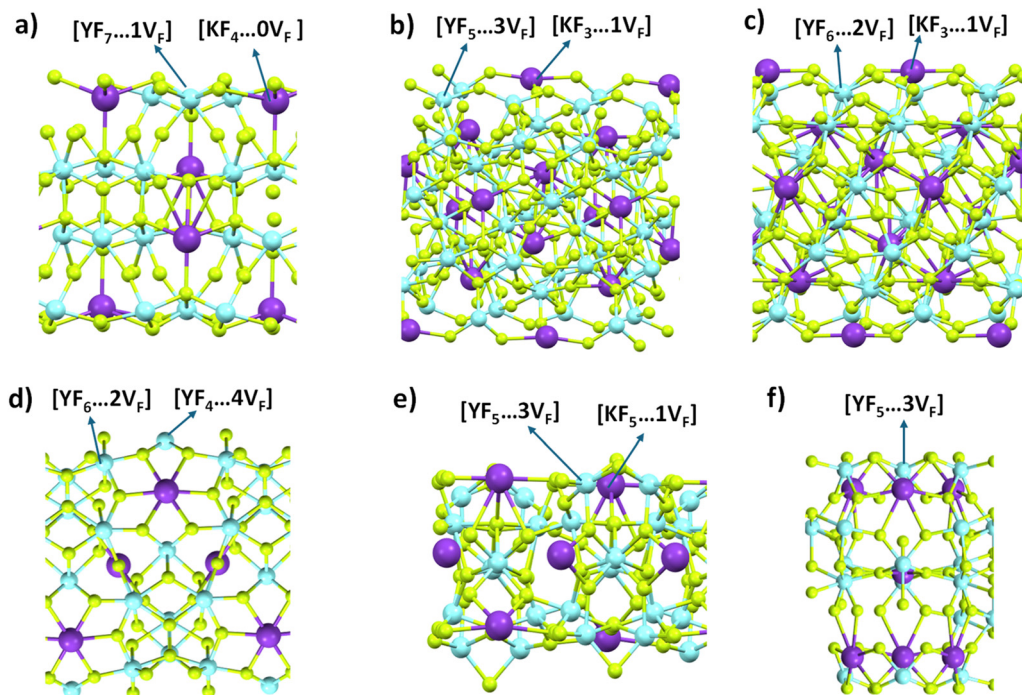


Fig. 7 Surface models of  $\alpha$ - $\text{KY}_3\text{F}_{10}$ : (a) (100), (b) (110), and (c) (111) and for  $\delta$ - $\text{KY}_3\text{F}_{10}$ : (d) (100), (e) (110), and (f) (111). The Y and K superficial clusters on the surfaces are shown.

clusters shows  $[\text{YF}_7]$  undercoordinated clusters for the (100) surface,  $[\text{YF}_5]$  clusters for the (110) and  $[\text{YF}_6]$  clusters for (111) surfaces of the  $\alpha$ - $\text{KY}_3\text{F}_{10}$  polymorph. In addition, the (110) and (111) surfaces also contain undercoordinated  $[\text{KF}_3]$  clusters. The fluorine broken bonds can be interpreted as fluorine vacancies and are written using the Kröger-Vink notation.<sup>60</sup> Instead, for the  $\delta$ - $\text{KY}_3\text{F}_{10}$  polymorph, undercoordinated  $[\text{YF}_4]$  and  $[\text{YF}_6]$  clusters compose the (100) surface, while the (110) and the (111) surfaces only present  $[\text{YF}_5]$  clusters. In addition, the (110) surface also contains undercoordinated  $[\text{KF}_5]$  clusters. All the studied surfaces are non-polar except for surface (e), which produces a non-zero dipole moment perpendicular to the surface with a high  $E_{\text{surf}}$  value. Therefore, the (100) surface has the lower surface energy ( $E_{\text{surf}}$ ) in  $\alpha$  and  $\delta$  polymorphs, which contain a low amount of undercoordinated Y and completely coordinated F sites. However,  $E_{\text{surf}}$  values are much higher for the  $\delta$  phase, due to a higher dangling bond value ( $D_{\text{B}} = 6.61 \text{ nm}^{-2}$ ) than in the  $\alpha$  polymorph ( $D_{\text{B}} = 3.34 \text{ nm}^{-2}$ ), as can be seen in Table 4.

Previously, we presented a framework that reveals how changing the values of  $E_{\text{surf}}$  opens a door to predicting and designing the complete map of available morphologies for a wide range of metals and metal oxides.<sup>61</sup> This procedure allows us to bridge a direct link between electron microscopy images and theoretical morphologies, which is applied here to complement and rationalize the experimental HRSEM images by combining the  $E_{\text{surf}}$  values of the exposed (100), (110), and (111) surfaces obtained by DFT calculations and Wulff construction. A map of available morphologies for both polymorphs is presented in Fig. 8, ordered by means of the

Table 4 Data of the thickness, area, undercoordinated clusters, and  $E_{\text{surf}}$  and  $D_{\text{B}}$  values for the studied surfaces of  $\alpha$  and  $\delta$  polymorphs

Surface	Thickness (Å)	Area (Å <sup>2</sup> )	$E_{\text{surf}}$ (J m <sup>-2</sup> )	Uncoordinated clusters	$D_{\text{B}}$ (nm <sup>-2</sup> )
$\alpha$ - $\text{KY}_3\text{F}_{10}$ (111)	13.33	114.59	0.92	$2[\text{YF}_6 \dots 2\text{V}_\text{F}]$ $2[\text{KF}_3 \dots 1\text{V}_\text{F}]$	5.23
(110)	12.97	114.59	1.15	$2[\text{YF}_5 \dots 3\text{V}_\text{F}]$ $2[\text{KF}_3 \dots 1\text{V}_\text{F}]$	6.98
(100)	12.08	59.85	0.43	$2[\text{YF}_7 \dots 1\text{V}_\text{F}]$	3.34
$\delta$ - $\text{KY}_3\text{F}_{10}$ (111)	12.89	104.79	4.40	$3[\text{YF}_5 \dots 3\text{V}_\text{F}]$	8.59
(110)	10.42	173.73	2.80	$2[\text{YF}_5 \dots 3\text{V}_\text{F}]$ $2[\text{KF}_5 \dots 1\text{V}_\text{F}]$	4.60
(100)	14.20	121.00	2.60	$2[\text{YF}_6 \dots 2\text{V}_\text{F}]$ $1[\text{YF}_4 \dots 4\text{V}_\text{F}]$	6.61

polyhedron energy ( $E_{\text{pol}}$ ) values. For the  $\alpha$  phase, an octahedral morphology was obtained as the most stable ( $0.23 \text{ J m}^{-2}$ ), resulting from the preferential stabilization of the (111) surface. Additional morphologies can be obtained by strategically modifying the  $E_{\text{surf}}$  values of specific surfaces and considering the contribution of each surface area, achieving truncated octahedral or cubic morphologies only with a lower increase in  $E_{\text{pol}}$  values. In contrast, for the  $\delta$  phase (Fig. 8b), both the octahedral and the cubic morphologies present low values of  $E_{\text{pol}}$  ( $1.60 \text{ J m}^{-2}$ ), although with  $E_{\text{pol}}$  values higher than that in the  $\alpha$  phase. The cubic morphology results from the preferential stabilization of the (100) surface, and three additional morphologies can be obtained with an increase in  $E_{\text{pol}}$  values up to  $2.0 \text{ J m}^{-2}$ .



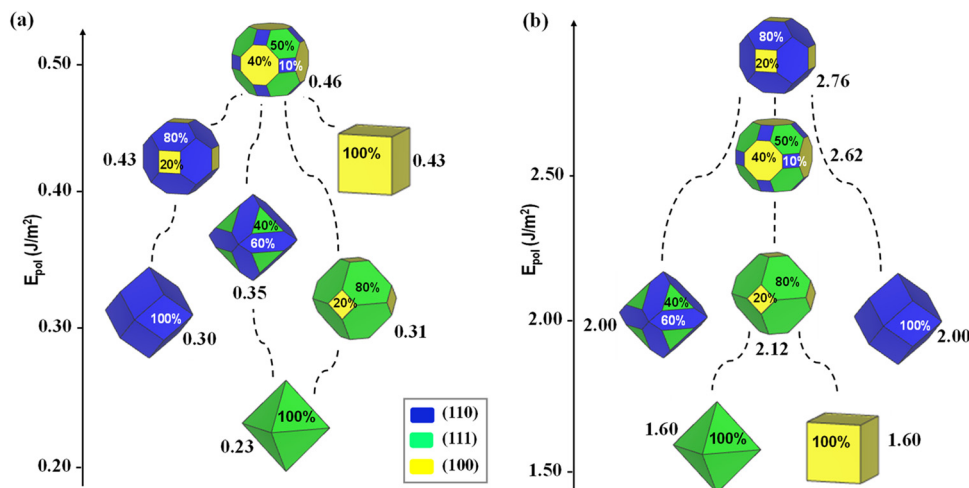


Fig. 8 Map of the available morphologies for (a)  $\alpha$ -KY<sub>3</sub>F<sub>10</sub> and (b)  $\delta$ -KY<sub>3</sub>F<sub>10</sub> polymorphs ordered by means of  $E_{\text{pol}}$  values.

Despite the distinct morphological differences, both polymorphs exhibited essentially cubic space groups. This indicates that the variation in the crystal morphology arises primarily from differences in crystal growth rates rather than from changes in the underlying lattice structure. Our analysis further reveals the pathways connecting experimental/theoretical morphologies, allowing us to make a direct link between variations of the values of  $E_{\text{surf}}$  and the morphology. Fig. 9(a) and (b) show the energy profiles connecting the morphologies obtained by HRSEM images and DFT calculations of  $\alpha$  and  $\delta$ -KY<sub>3</sub>F<sub>10</sub> polymorphs, respectively, which can be correlated with the Eu<sup>3+</sup> content. Confirmed by DFT calculations, cubic and octahedral are the most stable morphologies in the  $\delta$ -phase and with lower values in the  $\alpha$  phase (0.43 and 0.23 eV, respectively), suggesting the coexistence of both morphologies, as observed in the HRSEM image of S-20. In S-30 (and S-15), only octahedral and truncated octahedral morphologies coexist, having the latter  $E_{\text{pol}}$  values of 2.0 eV and 0.35 eV for the  $\alpha$  phase, respectively. Besides, the three morphologies (octahedral, cubic, and truncated octahedral) coexist in S-40, which can be connected from the cubic to the octahedral morphologies passing through the truncated octahedral without or with a barrier of 0.4 eV for the  $\alpha$  (Fig. 8a) or  $\delta$  (Fig. 8b) phases, respectively. This consistency validates the picture from our

model, where the values of the calculated  $E_{\text{surf}}$  of the exposed surfaces and  $E_{\text{pol}}$  are involved in each pathway. These findings underscore the importance of surface effects provoked by Eu<sup>3+</sup>-doping, and fit with experimental data reported for  $\alpha$ - and  $\delta$ -KY<sub>3</sub>F<sub>10</sub> polymorphs. Therefore, controlled surface synthesis is not only a rational route to study the relationship between the morphology and the surface structure-dependent properties but also a feasible approach for developing highly active materials to better customize their luminescent and photocatalytic functionalities. In this sense, it is expected that the  $\delta$  phase, with highly active surfaces exposed in its morphology ( $E_{\text{pol}}$  values much higher than that for the  $\alpha$  phase), shows superior optical and photocatalytic performance.

Understanding evolution guides the design of polymorphs of inorganic semiconductors by analyzing the effect of chemical/physical pressure, revealing structure–activity relationships that provide a theoretical basis for developing new materials. It can be argued that every technological breakthrough in this field stems from a profound understanding of its mechanism. The innovation of the current work is based on a comprehensive investigation of the polymorphism and morphology of  $\alpha$ - and  $\delta$ -KY<sub>3</sub>F<sub>10</sub> polymorphs induced by Eu<sup>3+</sup> doping (10–40%) and external pressure. It is important to note that there is a clear difference between chemical and physical

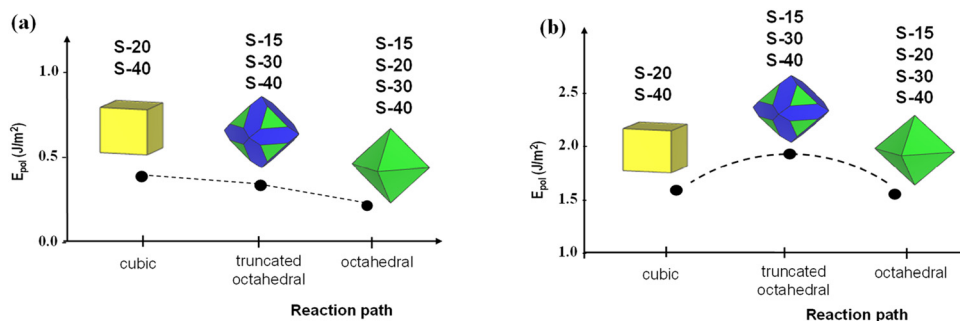


Fig. 9 Energy profiles connecting the morphologies obtained by HRSEM images and DFT calculations of the (a)  $\alpha$ -KY<sub>3</sub>F<sub>10</sub> and (b)  $\delta$ -KY<sub>3</sub>F<sub>10</sub> polymorphs.



pressure: the  $\text{Eu}^{3+}$  doping process regulates the  $\alpha$ -to- $\delta$  phase transition by a subtle modification of the local electronic structure of the  $[\text{EuF}_8]$  cluster at low values of  $\text{Eu}^{3+}$  doping, while this transition is achieved under negative pressure. The fundamental reasons behind this intriguing behavior were further rationalized by an in-depth integration of theoretical simulation (DFT calculations) and experimental verification (XRD, ICP-MS, FT-IR, and HRSEM) techniques, which is another important trend.

### III. Conclusions

The main conclusions of this work can be summarized as follows: (i) the integration of the experiments results with DFT calculations provides atomistic-level insights into the substitution process of  $\text{Y}^{3+}$  by  $\text{Eu}^{3+}$  under physical pressure to unravel the interplay among structural complexity, phase metastability, and morphological changes, (ii) the structural or electronic origin of the intricate relationship between chemical and physical pressures was successfully explained by subtle distortions in the local environment of  $\text{Eu}^{3+}$  at the  $[\text{EuF}_8]$  cluster in both the  $\alpha$  and  $\delta$  polymorphs, (iii) based on the DFT results, we reveal for the first time that small differences in the local arrangements of  $\text{Eu}^{3+}$  at the  $[\text{EuF}_8]$  cluster in both polymorphs follow quantum mechanical rules, which are conceptually connected to a model of energies and electronic configurations of 4f orbitals of  $\text{Eu}^{3+}$  in the coordination environment, (iv) the mechanism of the  $\alpha$  to  $\delta$  phase transition can be classified as a pressure-induced collapse caused by a symmetry reduction from  $C_{4v}$  to  $C_{2v}$  of the  $[\text{EuF}_8]$  cluster, (v) we estimate the enthalpy variation as a function of physical pressure and the phase transition from the  $\alpha$  to the  $\delta$  phase at  $-1.2$  GPa is maintained at 8.3% and 16.7% of  $\text{Eu}^{3+}$  doping, (vi) an extensive exploration of the stable configurations at different spin multiplicities for both polymorphs was performed at 8.3% and 16.7%  $\text{Eu}^{3+}$ , and the DOS analysis reveals localized intermediate states contributed by Eu 4f orbitals, significantly narrowing the effective band gap of both polymorphs, which could enhance optical absorption in the visible region, (vii) a correlation between the relative stability of  $\text{Eu}^{3+}$ -doped  $\alpha$ - and  $\delta$ - $\text{KY}_3\text{F}_{10}$  polymorphs and the 4f orbital occupancy at the  $[\text{EuF}_8]$  cluster with  $C_{4v}$  and  $C_{2v}$  symmetries, respectively, is delineated, as a result of the meticulous manipulations of both chemical and physical pressures at the atomic level, and (viii) by employing the values of surface and polyhedron energies derived from the DFT calculations and Wulff construction, a more comprehensive picture of the changes in the morphology can be obtained, where these calculations were sufficient for an adequate description of the different pathways connecting the spherical, octahedral, cubic and truncated octahedra of the observed morphologies.

Taken together, the novelty of the present findings lies in the disentanglement of a coupling mechanism among chemical and pressure effects and the local structure of the  $[\text{EuF}_8]$  cluster, providing an understanding of the structural

and electronic properties of  $\alpha$ - and  $\delta$ - $\text{KY}_3\text{F}_{10}$  polymorphs, as host materials, through the controlled substitution of  $\text{Y}^{3+}$  by  $\text{Eu}^{3+}$ . The importance of the trapped  $\delta$  metastable phase in the  $\text{KY}_3\text{F}_{10}$  matrix is highlighted to tune the physical properties and soften the synthesis conditions in a cost-effective way. By bridging atomic-scale simulations with experimental observables, the comprehensive discussion aims to provide theoretical guidance for developing  $\alpha$ - and  $\delta$ - $\text{KY}_3\text{F}_{10}$  polymorphs, which might be relevant for a precise polymorphic transition with tunable response characteristics.

### Conflicts of interest

There are no conflicts to declare.

### Data availability

The data supporting this article have been included as part of the supplementary information (SI). Supplementary information is available. See DOI: <https://doi.org/10.1039/d6tc00645k>.

### Acknowledgements

S. C. S. L., M. J. A., and L. G. thank Universitat Jaume I (project UJI-B2022-56), Ministerio de Ciencia, Innovación y Universidades (project PID2022-141089NB-I00), and Generalitat Valenciana (CIAICO/2024/94) for financially supporting this research. S. C. S. L. has been funded by Generalitat Valenciana (CIAPOS/2022/148) and E. O. G. has been funded by Generalitat Valenciana (CIAPOS/2022/162). H. B. M. and E. C. thank Ministerio de Ciencia, Innovación y Universidades (Project PID2024-158224NB-I00 funded by MICIU/AEI/10.13039/501100011033 and by ERDF/EU) and Universitat Jaume I (project GACUJIMA/2025/10).

### References

- 1 B. K. Saha, N. K. Nath and R. Thakuria, *Chem. Rec.*, 2023, **23**, e202200173.
- 2 D. Gentili, M. Gazzano, M. Melucci, D. Jones and M. Cavallini, *Chem. Soc. Rev.*, 2019, **48**, 2502–2517.
- 3 P. F. McMillan, *Chem. Soc. Rev.*, 2006, **35**, 855–857.
- 4 A. Katrusiak, *Acta Crystallogr., Sect. B: Struct. Sci., Cryst. Eng. Mater.*, 2019, **75**, 918–926.
- 5 K. P. Hilleke, T. Bi and E. Zurek, *Appl. Phys. A: Mater. Sci. Process.*, 2022, **128**, 441.
- 6 M. Miao, Y. Sun, E. Zurek and H. Lin, *Nat. Rev. Chem.*, 2020, **4**, 508–527.
- 7 B. C. Barnes, J. K. Brennan, E. F. C. Byrd, S. Izvekov, J. P. Larentzos and B. M. Rice, in *Computational Approaches for Chemistry Under Extreme Conditions*. ed. N. Goldman, Springer, 2019, vol. 28.
- 8 E. Zurek and W. Grochala, *Phys. Chem. Chem. Phys.*, 2015, **17**, 2917–2934.



- 9 F. Zeller, C. Hsieh, W. Dononelli and T. Neudecker, *Wiley Interdiscip. Rev.: Comput. Mol. Sci.*, 2024, **14**, e1708.
- 10 A. Parija, G. R. Waetzig, J. L. Andrews and S. Banerjee, *J. Phys. Chem. C*, 2018, **122**, 25709–25728.
- 11 P. A. Maggard, *Acc. Chem. Res.*, 2021, **54**, 3160–3171.
- 12 M. Biswas and H. Nishinaka, *APL Mater.*, 2022, **10**, 060701.
- 13 M. Aykol, S. S. Dwaraknath, W. Sun and K. A. Persson, *Sci. Adv.*, 2025, **4**, eaaq0148.
- 14 D. Zhao, M. Wang, G. Xiao and B. Zou, *J. Phys. Chem. Lett.*, 2020, **11**, 7297–7306.
- 15 D. D. Le Pevelen and G. E. Tranter, *Encyclopedia of spectroscopy and spectrometry*, Academic Press, Oxford, 2017, pp. 750–761.
- 16 K. Lin, Q. Li, R. Yu, J. Chen, J. P. Attfield and X. Xing, *Chem. Soc. Rev.*, 2022, **51**, 5351–5364.
- 17 H. H. Osman, M. A. Salvadó, P. Pertierra, J. Engelkemier, D. C. Fredrickson and J. M. Recio, *J. Chem. Theory Comput.*, 2018, **14**, 104–114.
- 18 A. Lobato, H. H. Osman, M. A. Salvado, P. Pertierra, A. Vegas, V. G. Baonza and J. M. Recio, *Inorg. Chem.*, 2020, **59**, 5281–5291.
- 19 J. M. Recio, A. Lobato, H. H. Osman, M. A. Salvadó and A. Vegas, *Comprehensive Inorganic Chemistry III*, Elsevier, 2023, vol. 1, pp. 238–261.
- 20 E. O. Gomes, A. F. Gouveia, L. Gracia, A. Lobato, J. M. Recio and J. Andres, *J. Phys. Chem. Lett.*, 2022, **13**, 9883–9888.
- 21 H. L. Huang, C. Chae, J. M. Johnson, A. Senckowski, S. Sharma, U. Singiseti and J. Hwang, *APL Mater.*, 2023, **11**(6), 061113.
- 22 M. Govindhan and K. Sukumar, *J. Power Sources*, 2025, **658**, 238287.
- 23 H. H. Osman, A. Otero-De-la-Roza, P. Rodriguez-Hernández, A. Munoz and F. J. Manjon, *J. Mater. Chem. C*, 2024, **12**, 10447–10474.
- 24 H. H. Osman, P. Rodríguez-Hernández, A. Muñoz and F. J. Manjón, *J. Mater. Chem. C*, 2025, **13**, 3774–3803.
- 25 A. F. Gouveia, M. Assis, L. K. Ribeiro, E. O. Gomes, M. D. Teodoro, E. Longo and J. Andres, *J. Mater. Chem. C*, 2025, **13**, 6788–6798.
- 26 P. F. Pereira, C. C. De Foggi, A. F. Gouveia, I. M. Pinatti, L. A. Cabral, E. Guillaumon and J. Andrés, *Int. J. Mol. Sci.*, 2022, **23**, 10589.
- 27 R. Alvarez-Roca, A. F. Gouveia, C. C. De Foggi, P. S. Lemos, L. Gracia, L. F. Da Silva and J. Andres, *Inorg. Chem.*, 2021, **60**, 1062–1079.
- 28 J. Andrés, L. Gracia, A. F. Gouveia, M. M. Ferrer and E. Longo, *Nanotechnology*, 2015, **26**, 405703.
- 29 M. M. Ferrer, A. F. Gouveia, L. Gracia, E. Longo and J. Andrés, *Model. Simul. Mater. Sci. Eng.*, 2016, **24**, 25007.
- 30 A. F. Gouveia, L. Gracia, E. Longo, M. A. San-Miguel and J. Andrés, *Comput. Mater. Sci.*, 2021, **188**, 110217.
- 31 Z. Mazej and E. Goresnik, *Inorg. Chem.*, 2022, **61**, 10587–10597.
- 32 N. Rybin, I. Chepkasov, D. Y. Novoselov, V. I. Anisimov and A. R. Oganov, *J. Phys. Chem. C*, 2022, **126**, 15057–15063.
- 33 P. P. Fedorov, V. V. Semashko and S. L. Korableva, *Inorg. Mater.*, 2022, **58**, 235–257.
- 34 N. I. Sorokin and D. N. Karimov, *Phys. Solid State*, 2021, **63**, 1821–1832.
- 35 J. W. De Wit, T. P. van Swieten, M. A. van de Haar, A. Meijerink and F. T. Rabouw, *Adv. Opt. Mater.*, 2023, **2202974**, 1–7.
- 36 Y. Zhang, W. Ying, J. He, X. Fan, S. Xu, J. Gu and S. Liu, *Dalton Trans.*, 2023, **52**, 2948–2955.
- 37 C. Cressoni, F. Vurro, E. Milan, M. Muccilli, F. Mazzer, M. Gerosa and A. Speghini, *ACS Appl. Mater. Interfaces*, 2023, **15**, 12171–12188.
- 38 J. L. B. Martin, P. S. Solanki, S. Balabhadra, Y. Alizadeh, M. F. Reid and J. P. Wells, *J. Lumin.*, 2021, **233**, 117923.
- 39 K. de Oliveira Lima, L. F. dos Santos, M. T. de Melo, A. C. Tedesco, R. R. Gonçalves, P. Gredin and M. Mortier, *Mater. Today Commun.*, 2021, **28**, 102553.
- 40 P. S. Solanki, S. Balabhadra, M. F. Reid, V. B. Golovko and J. R. Wells, *ACS Appl. Nanomater.*, 2021, **4**, 5696–5706.
- 41 P. Serna-Gallén, *Crystals*, 2024, **14**, 762.
- 42 A. P. Ayala, M. A. S. Oliveira, J.-Y. Gesland and R. L. Moreira, *J. Phys.: Condens. Matter*, 1998, **10**, 5161.
- 43 ed. P. Villars and K. Cenzual, KY3F10 Crystal Structure: Datasheet from 'PAULING FILE Multinaries Edition – 2012 in SpringerMaterials ([https://materials.springer.com/isp/crystallographic/docs/sd\\_0552093](https://materials.springer.com/isp/crystallographic/docs/sd_0552093)).
- 44 D. J. M. Bevan and S. E. Lawton, *Acta Crystallogr., Sect. B*, 1986, **42**, 55–58.
- 45 P. Serna-Gallén, H. Beltrán-Mir and E. Cordoncillo, *Opt. Laser Technol.*, 2021, **136**, 106734.
- 46 P. Serna-Gallén, H. Beltrán-Mir and E. Cordoncillo, *J. Alloys Compd.*, 2021, **883**, 160847.
- 47 P. Serna-Gallén, H. Beltrán-Mir and E. Cordoncillo, *J. Mater. Res. Technol.*, 2021, **15**, 6940–6946.
- 48 M. Runowski, N. Stopikowska, S. Goderski and S. Lis, *J. Alloys Compd.*, 2018, **762**, 621–630.
- 49 M. Xin, *Opt. Laser Technol.*, 2024, **170**, 110271.
- 50 K. S. Prichisly, *Crystals*, 2025, **15**, 500.
- 51 P. Serna-Gallén, H. Beltrán-Mir and E. Cordoncillo, *Ultrason. Sonochem.*, 2022, **87**, 106059.
- 52 A. J. Garza and G. E. Scuseria, *J. Phys. Chem. Lett.*, 2016, **7**, 4165–4170.
- 53 J. P. Perdew, W. Yang, K. Burke, Z. Yang, E. K. Gross, M. Scheffler and A. Görling, *Proc. Natl. Acad. Sci. U. S. A.*, 2017, **114**, 2801–2806.
- 54 P. Serna-Gallén, H. Beltrán-Mir and E. Cordoncillo, *CrystEngComm*, 2023, **25**, 5918–5931.
- 55 R. D. Shannon, *Acta Crystallogr.*, 1976, **A32**, 751–767.
- 56 A. Jain, S. P. Ong, G. Hautier, W. Chen, W. D. Richards, S. Dacek and K. A. Persson, *APL Mater.*, 2013, **1**, 11002.
- 57 ed. D. W. Oxtoby, H. P. Gillis, A. Campion, *Cengage Learn*, Belmont, CA, 2016, 8th edn.
- 58 J. D. Lee, *Concise inorganic chemistry*, John Wiley & Sons, 2008.
- 59 N. G. Macedo, A. F. Gouveia, R. A. Roca, M. Assis, L. Gracia, J. Andres and E. Longo, *J. Phys. Chem. C*, 2018, **122**, 8667–8679.
- 60 F. A. Kröger and H. I. Vink, *Solid State Phys.*, 1956, **3**, 307–435.
- 61 M. M. Ferrer, A. F. Gouveia, L. Gracia, E. Longo and J. Andrés, *Model. Simul. Mater. Sci. Eng.*, 2016, **24**, 025007.

